Electronic correlation effects in transition-metal sulfides

2003 J. Phys.: Condens. Matter 15 979

(http://iopscience.iop.org/0953-8984/15/6/325)

INSTITUTE OF PHYSICS PUBLISHING JOURNAL OF PHYSICS: CONDENSED MATTER

J. Phys.: Condens. Matter **15** (2003) 979–996 PII: S0953-8984(03)53786-9

Electronic correlation effects in transition-metal sulfides

A Rohrbach, J Hafner and G Kresse

Institut für Materialphysik and Centre for Computational Material Science, Universität Wien, Sensengasse 8/12, A-1090 Wien, Austria

Received 23 September 2002
Published 3 February 2003
Online at stacks.iop.org/JPhysCM/15/979

Abstract

Density-functional studies of structural and electronic properties of transition-metal sulfides formed by 3d transition metals, based on the local spin-density approximation and including non-local corrections to the exchange–correlation functional (generalized gradient approximation), have demonstrated the importance of magneto-volume effects and magneto-structural effects, but could not achieve full agreement with experiment. A further improvement is to consider electronic correlation effects due to tightly bound and localized d-states on the transition metal atoms. With the DFT + U method used in this work, these correlation effects are taken in account and yield improved predictions for volume, magnetic moment, exchange splitting and bandgap. For MnS the semiconducting gap is correctly predicted, and for MnS_2 the high-spin AFM type-III state can be stabilized over the low-spin state. For FeS even weak correlation effects lead to better predictions for the semiconducting gap, volume and magnetic moment.

1. Introduction

Transition-metal sulfides (TMSs) form an important class of inorganic compounds with manifold applications in industry, ranging from catalysis over lubrication to corrosion protection. In recent years, the use of TMSs as catalysts for the hydro-desulfurization of fuels has been studied with particular interest [1–3]. It was shown that whereas for the 4d and 5d TMSs the catalytic activity reaches a maximum for an approximately half-filled d band, the activity of the homologous 3d compounds remains very low throughout the series.

Raybaud *et al* [2] have performed a comprehensive investigation of the structural, cohesive and electronic properties of more than 30 TMSs in the local density approximation (LDA). Their calculations demonstrated that the overbinding tendency of the LDA (prediction of too small atomic volumes and too large cohesive energies) is particularly pronounced for the TMSs. For the 4d and 5d TMSs, the overbinding is largely corrected by including non-local corrections in the form of a generalized gradient approximation (GGA). For the 3d TMSs, Hobbs and

Hafner [5] reported the existence of strong magneto-structural effects. However, the local spin-density approximation (LSDA) supplemented by gradient corrections does not lead to a satisfactory description of the physical properties for all 3d TMSs; CrS is well described as an itinerant antiferromagnet with a substantial magneto-volume effect (7% increase due to magnetic ordering), MnS is correctly predicted to be an antiferromagnetic semiconductor with a very large magneto-volume effect (≈21%), but the width of the semiconducting gap, the exchange splitting and the magnetic moments are underestimated (even the equilibrium volume is still too small by about 7%). This indicates the importance of intra-atomic correlation effects similar to those found to those found in the 3d monoxides [6]. In MnS_2 the spin-polarized GGA calculations predict a stable antiferromagnetic low-spin ground state and a metastable high-spin state at expanded volume. The structural parameters for this high-spin state are much closer to those observed experimentally, and it was suggested that the high-spin state could possibly be stabilized by rather strong intra-atomic correlations.

FeS undergoes phase transitions from the troilite to the MnP-type and NiAs-type structures under compression, which is correctly predicted by the LSDA + GGA calculations. Important discrepancies between theory and experiments exist nevertheless: (i) the absence of a semiconducting gap, too small exchange splitting, (ii) too low magnetic moment and (iii) too small equilibrium volume. FeS_2 is correctly described as a semiconductor, CoS and CoS_2 are metallic and correctly described as non-magnetic and as a weak itinerant ferromagnet, respectively. NiS and NiS_2 are antiferromagnetic Mott insulators, but predicted to be non-magnetic and metallic in LSDA calculations.

Hence it appears that the TMSs are intermediate between the transition-metal oxides, whose properties are determined by strong correlation effects [6], and transition-metal selenides, showing a variety of electronically induced structural phase transitions [13]. An approximate description of strong intra-atomic correlation effects is provided by the DFT + U approach where on-site Coulomb and exchange interactions described in an unrestricted Hartree–Fock approximation are added to the DFT Hamiltonian [12]. In the present work we apply the DFT + U as formulated by Dudarev *et al* [9] to the investigation of the structural and electronic properties of several 3d TMSs. Both the LDA and the GGA are used as a starting point. Our paper is organized as follows: in section 2 we review very briefly the foundation of the DFT + U method and we describe its implementation in the Vienna *ab initio* simulation package VASP. Sections 3–5 describe the application to MnS, MnS_2 and FeS and we summarize in section 6.

2. Theoretical methods

2.1. DFT + U method

Transition-metal compounds like NiO experience a strong on-site Coulomb repulsion amongst Ni 3d electrons due to the narrow d bandwidth, which is not correctly described in a spin-polarized DFT treatment. This error can be corrected with the DFT + U method, which is a combination of the DFT and a Hubbard Hamiltonian for the Coulomb repulsion. For the present calculations we use a simple DFT + U version, proposed by Dudarev *et al* in [9]. It is based on a model Hamiltonian with the form [10]

$$\hat{H} = \frac{U}{2} \sum_{m,m',\sigma} \hat{n}_{m,\sigma} \hat{n}_{m',-\sigma} + \frac{(U-J)}{2} \sum_{m \neq m',\sigma} \hat{n}_{m,\sigma} \hat{n}_{m',\sigma}; \tag{1}$$

$\hat{n}_{m\sigma}$ is the operator yielding the number of electrons occupying an orbital with magnetic quantum number m and spin σ at a particular site.

The Coulomb repulsion is characterized by a spherically averaged Hubbard parameter U describing the energy increase for placing an extra electron on a particular site, $U = E(\mathrm{d}^{n+1}) + E(\mathrm{d}^{n-1}) - 2E(\mathrm{d}^{n})$, and a parameter J representing the screened exchange energy. While U depends on the spatial extent of the wavefunctions and on screening, J is an approximation of the Stoner exchange parameter and almost constant, $\sim$1 eV [11]. The Mott–Hubbard Hamiltonian includes energy contributions already accounted for by the DFT functional. To correct for this 'double-counting', equation (1) is evaluated in the limit of integer occupancies and subtracted from the DFT energy to obtain the spin-polarized DFT + U energy functional [9, 11]. A simple functional is obtained after some straightforward algebra [9]:

$$E_{DFT+U} = E_{DFT} + \frac{U-J}{2}\sum_{m\sigma}(n_{m\sigma} - n_{m\sigma}^2). \tag{2}$$

This energy functional is yet not invariant with respect to a unitary transformation of the orbitals. A formulation given by Lichtenstein *et al* [12] replaces the number operator by the on-site density matrix ρ_{ij}^{σ} of the d electrons to obtain a rotationally invariant energy functional. In the present case this yields the functional [9]

$$E_{DFT+U} = E_{DFT} + \frac{U-J}{2}\sum_{\sigma}\mathrm{Tr}[\rho^{\sigma} - \rho^{\sigma}\rho^{\sigma}]. \tag{3}$$

The interpretation of this DFT+U functional is particularly simple. In the limit of an idempotent on-site occupancy matrix ρ^{σ}

$$\rho^{\sigma\,2} = \rho^{\sigma}$$

the DFT+U functional yields exactly the same energy as the DFT functional $E_{DFT+U} = E_{DFT}$. The second term in equation (3) forces this idempotency. If $U > J$, the term is positive definite, since the eigenvalues ϵ_i of the on-site occupancy matrix can vary only between zero and unity.

$$\rho^{\sigma} - \rho^{\sigma}\rho^{\sigma} = \sum_i \epsilon_i^{\sigma} - \epsilon_i^{\sigma\,2} > 0$$

where the sum on the right-hand side is over all eigenvalues ϵ_i of the on-site occupancy matrix ρ^{σ}. Hence the second term in equation (3) can be interpreted as a positive definite penalty function driving the on-site occupancy matrices towards idempotency. The DFT + U energy obtained in this manner is always larger than the DFT energy. The 'strength' of the penalty function is parametrized by a *single* parameter $U - J$. A larger $U - J$ forces a stricter observance of the on-site idempotency. This is achieved by lowering the one-electron potential locally for a particular metal d orbital and in turn reducing the hybridization with e.g. O atoms: the one-electron potential is given by the functional derivative of the total energy with respect to the electron density, i.e. in a matrix representation

$$V_{ij}^{\sigma} = \frac{\delta E_{DFT+U}}{\delta\rho_{ij}^{\sigma}} = \frac{\delta E_{DFT}}{\delta\rho_{ij}^{\sigma}} + (U-J)\left[\frac{1}{2}\delta_{ij} - \rho_{ij}^{\sigma}\right]. \tag{4}$$

It is recognized that filled d orbitals which are localized on one particular site are moved to lower energies, by $-(U-J)1/2$, whereas empty d orbitals are raised to higher energies by $(U-J)1/2$.

2.2. Implementation within the projector-augmented wave method

The DFT + U method is implemented in the projector-augmented wave (PAW) method as described by Bengone *et al* [16]. In the PAW method, the all-electron wavefunction Ψ_n is related to the pseudo-wavefunction $\tilde{\Psi}_n$ through a linear transformation [14, 15]:

$$|\Psi_n\rangle = |\tilde{\Psi}_n\rangle + \sum_i (|\phi_i\rangle - |\tilde{\phi}_i\rangle)\langle\tilde{p}_i|\tilde{\Psi}_n\rangle. \tag{5}$$

The index i is a shorthand for the atomic site $\boldsymbol{R}$, the angular momentum numbers $L = l, m$ and an additional index n referring to the reference energy ϵ_{nl}. The all-electron partial waves ϕ_i are solutions of the Schrödinger equation for a spherical symmetric reference atom, and the pseudo partial waves $\tilde{\phi}_i$ are equivalent to the AE partial waves outside a core radius r_c and match continuously onto $\tilde{\phi}_i$ inside the core radius. The projector functions $\tilde{p}_i$ are dual to the partial waves:

$$\langle \tilde{p}_i | \tilde{\phi}_j \rangle = \delta_{ij}.$$

Starting from equation (5) it is possible to show that the AE charge density is given by a sum of three terms in the PAW method (for details we refer to [14] and [15]):

$$n(\boldsymbol{r}) = \tilde{n}(\boldsymbol{r}) + n^1(\boldsymbol{r}) - \tilde{n}^1(\boldsymbol{r}). \tag{6}$$

Here, $\tilde{n}$ is the soft pseudo charge density related directly to the pseudo-wavefunctions $\tilde{\Psi}_n$. The on-site charge densities $n^1(\boldsymbol{r})$ and $\tilde{n}^1(\boldsymbol{r})$ are only defined inside spheres with radius r_c centred around each atom (PAW spheres). For the densities $n^1(\boldsymbol{r})$ and $\tilde{n}^1(\boldsymbol{r})$ the following defining equations are obtained:

$$n^1(\boldsymbol{r}) = \sum_{(i,j)} \rho_{ij}^{PAW} \langle \phi_i | \boldsymbol{r} \rangle \langle \boldsymbol{r} | \phi_j \rangle, \tag{7}$$

and

$$\tilde{n}^1(\boldsymbol{r}) = \sum_{(i,j)} \rho_{ij}^{PAW} \langle \tilde{\phi}_i | \boldsymbol{r} \rangle \langle \boldsymbol{r} | \tilde{\phi}_j \rangle. \tag{8}$$

The matrix ρ_{ij}^{PAW} describes the occupancies of each augmentation channel (i, j), and is calculated by multiplication of the pseudo density operator with the projector functions from the left and right:

$$\rho_{ij}^{PAW} = \sum_n f_n \langle \tilde{\Psi}_n | \tilde{p}_i \rangle \langle \tilde{p}_j | \tilde{\Psi}_n \rangle. \tag{9}$$

For a complete set of partial waves, the density $n^1(\boldsymbol{r})$ is exactly equivalent to the exact all-electron charge density within the PAW sphere,

$$n(\boldsymbol{r}) = n^1(\boldsymbol{r})$$

which is the crucial relation on which the present implementation of the DFT + U method rests.

To derive the PAW + U method, one needs to define the orbital density matrix $\rho_{mm'}$ entering equation (3). The natural definition is based on the AE charge density inside the PAW augmentation spheres, $n^1(\boldsymbol{r})$, which can be written more explicitly as

$$n^1(\boldsymbol{r}) = \sum_{(lmn),(l'm'n')} \rho^{\mathrm{PAW}}_{(lmn),(l'm'n')} \langle \phi_{lmn} | \boldsymbol{r} \rangle \langle \boldsymbol{r} | \phi_{l'm'n'} \rangle,$$

with the restriction to l and $l' = 2$, one can therefore relate the on-site density matrix $\rho_{mm'}$ to the PAW on-site occupancy matrix $\rho^{PAW}_{(lmn),(lm'n')}$ through

$$\rho_{mm'} = \sum_{nn'} \rho^{PAW}_{(lmn),(lm'n')} \langle \phi_{lmn} | \phi_{l'm'n'} \rangle.$$

This establishes the crucial link between the PAW and the DFT + U method. For further details the reader is referred to [16].

2.3. Further computational details

The calculations in this work were performed with the Vienna *ab initio* simulation package, VASP [15, 20–23]. VASP is a first-principles plane-wave code, treating exchange and correlation in the DFT scheme. The PAW method [14] in the implementation of Kresse and Joubert [15] is used to describe the electron–ion interaction. At the level of the LDA, the exchange–correlation functional proposed by Perdew and Zunger [24] (based on the quantum Monte Carlo calculations of Ceperley and Alder [25]) is used. Generalized gradient corrections are added in the form of the Perdew–Wang [27] functional. For spin-polarized calculations, the spin interpolation of Vosko *et al* [26] was used. The Kohn–Sham equations are solved via iterative matrix diagonalization based on the minimization of the norm of the residual vector to each eigenstate and optimized charge- and spin-mixing routines [28–30].

To sample the band structure, the Brillouin zone integration is performed using Monkhorst–Pack grids [31]. The unit cells are usually extended in one direction due to symmetry breaking in antiferromagnetic set-ups. k-point grids varying from $3 \times 3 \times 1$ to $6 \times 6 \times 4$ were used. The densities of states (DOSs) were calculated using the linear tetrahedron method. For the calculation of the total energy as a function of volume, a Gaussian-smearing approach with $\sigma = 0.2$ eV was used. The plane-wave cut-off was fixed to 330 eV. The DFT + U version of Dudarev *et al* [9] described above was used for all calculations. Since the DFT + U functional depends only on the difference $U - J$, J was kept fixed to 1 eV during all calculations. The $U - J = 0$ case represents the DFT limit.

3. Mn monosulfide

MnS takes the NaCl structure with an experimental unit cell volume of 17.99 Å^3. It is a type-II antiferromagnet with a magnetic moment of $\mu_{\mathrm{Mn}} = 4.54\ \mu_B$, which is near the saturation value of 5 μ_B according to the Hund rule. MnS is a Mott–Hubbard insulator with a bandgap of about 2.7 eV. The exchange splitting is around 8 eV.

Spin-polarized calculations with the GGA method [5] have stabilized an antiferromagnetic type-II ground state with a magnetic moment $\mu_{\mathrm{Mn}} = 4.08\ \mu_B$ but with $\Omega = 16.79$ Å^3 the volume was underestimated by 7%. The bandgap of about 1 eV and the exchange splitting of 4.2 eV are too small compared to experimental values. Non-spin-polarized calculations by Raybaud *et al* [2] had underestimated the volume by 33% for LSDA and by 27% for GGA. Taking into account spin polarization already leads to a substantial improvement in the GGA results, showing the existence of a strong magneto-volume effect. Hartree–Fock (HF) calculations by Hines *et al* [32] gave an antiferromagnetic type-II ground state and overestimated both the equilibrium volume (by 12%) and the magnetic moment at the optimized structure ($\mu_{\mathrm{Mn}} = 4.92\ \mu_B$). The exchange splitting was grossly overestimated with the filled spin-up Mn 3d band at 8 eV below the Fermi level and the lower edge of the empty spin-down Mn 3d band at +11 eV. More recent HF calculations by Tappero *et al* [33, 34] have shown that correlation corrections to the HF energy could reduce the volume mismatch by 2.5% and the large bandgap from 11 to 1.5 eV, whereas the magnetic moment remained at values very close to the Hund limit of 5 μ_B.

Our DFT + U calculations were done with a fixed exchange parameter $J = 1$; the on-site Coulomb interaction U was varied from 1 to 10 eV, using both the LDA and the GGA as a starting point.

These results show evidence for the necessity of taking the intra-atomic correlations between the d electrons into account. Increasing the U parameter, one can observe that

bandgap, magnetic moment and volume increase (see figure 1). In the LDA + U, the experimental value of the volume cannot be reached even with large U ($\sim$10 eV). But bandgap and magnetic moment reach a break-even with experiment for $U - J$ between 5 and 8 eV (see figure 1). For $U - J = 8$ eV, the volume is increased by $\sim$10% compared to the LDA, still underestimating the experiment by 3%. This comparison suggests that a reasonable choice for the U parameter (J is fixed at 1 eV) in the LDA + U lies between 6 and 7 eV, which is less than values usual for strongly correlated transition metal oxides. For MnO the appropriate choice is $U - J = 10$ eV (see [5]). As the GGA already produces a larger atomic volume, a slightly increased magnetic moment and a small energy gap, a significantly weaker on-site Coulomb interaction is sufficient to close the gap between theory and experiment: $U - J \approx 2$ eV for the volume, $U - J = 3$ eV for the magnetic moment—for the bandgap, complete agreement with experiment can only be reached for very large U. Hence it appears that within the semiempirical DFT + U approach, whether in the form of a LDA + U or a GGA + U, not all physical properties can be fixed with a single value of the on-site interaction. However, the bandgap problem and the electronic structure deserve further investigation. The density of states for both occupied and empty bands is displayed in figure 2. We find that with increasing U both the occupied majority-spin Mn 3d band and the empty minority-spin band are shifted away from the Fermi level, increasing the exchange splitting. However, as the S p band hybridizing with the occupied Mn 3d states is not affected by the Mn on-site interactions, the bandgap widens only moderately. In both the LDA + U and the GGA + U the electronic DOS for $U - J = 6$ eV shows a 3d exchange splitting of $\sim$9 eV and a bandgap of around $\sim$2.2 eV (see figure 2). While the bandgap is slightly lower than the experimental value, the exchange splitting (defined in terms of the positions of the most prominent peaks of the DOS of the majority and minority bands) is overestimated as indicated by the location of the occupied 3d states in comparison with measured UPS spectra [35]. UPS spectra measured at photon energies of 40.8 eV place the peak of the 3d band at -3.7 eV, whereas the peak of the calculated density of states is located at -5 eV. Figure 3 shows a comparison of the experimental and calculated UPS spectra; the theoretical UPS spectrum is calculated as a weighted average of the partial DOSs, using the photoionization cross sections of Yeh and Landau [36]. Good agreement between theory and experiment can only be reached for a relatively weak on-site interaction of $U - J \sim 2$ eV; for stronger on-site interactions the dominant peak is shifted to too high binding energies. However, it must also be pointed out that the intensity at the lower edge of the conduction band is rather flat—it is therefore plausible that the calculated gap is narrower than the experimental values determined by optical or spectroscopic techniques.

Our results for MnS illustrate a dilemma quite characteristic of the semiempirical DFT + U approaches. Although qualitatively the Coulomb corrections go in the proper direction, different values of U are required to fit different quantities. This problem is particularly acute in the LDA + U where the values of the on-site potential required to achieve agreement with experiment increase from the d-band position ($U \sim 3.5$ eV) to the magnetic moment ($U \sim 5$ eV), the bandgap ($U \sim$ 8–9 eV) and the equilibrium volume ($U \geqslant 9$ eV). In the GGA these discrepancies are less pronounced: $U - J \sim 3 \pm 1$ eV leads to reasonable predictions for atomic volume, magnetic moment, exchange splitting and d-band position—only a bandgap in agreement with experiment seems to require a much larger U. This remaining deficiency has to be blamed on the fact that pure on-site corrections leave the S states almost unaffected: on going from the GGA to the GGA + U, the character of the bandgap changes from an Mn d/d gap to a S p/Mn d gap (cf our figure 2 with 3 in [5]). Altogether the GGA + U is found to be largely superior to the LDA + U.

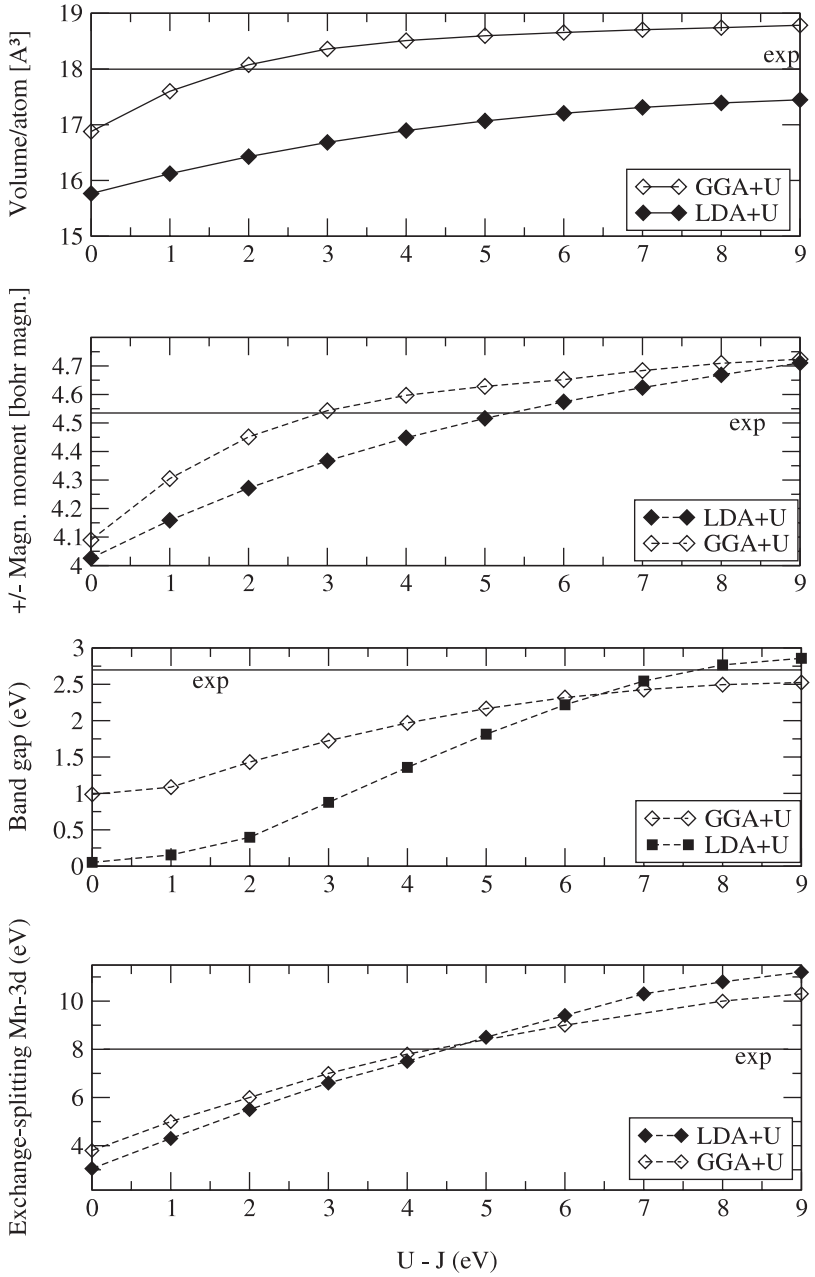

Figure 1. Atomic volume, magnetic moment, bandgap and exchange splitting in MnS, calculated in the LDA + U and GGA + U approximations as a function of the on-site Coulomb interaction. Experimental values are indicated by horizontal lines.

4. Mn disulfide

According to experiment, MnS_2 is a Mott insulator with a gap of 1 eV (see [40]) and crystallizes in a pyrite (FeS_2-type) crystal structure with a volume of 18.83 Å/atom and a bulk modulus

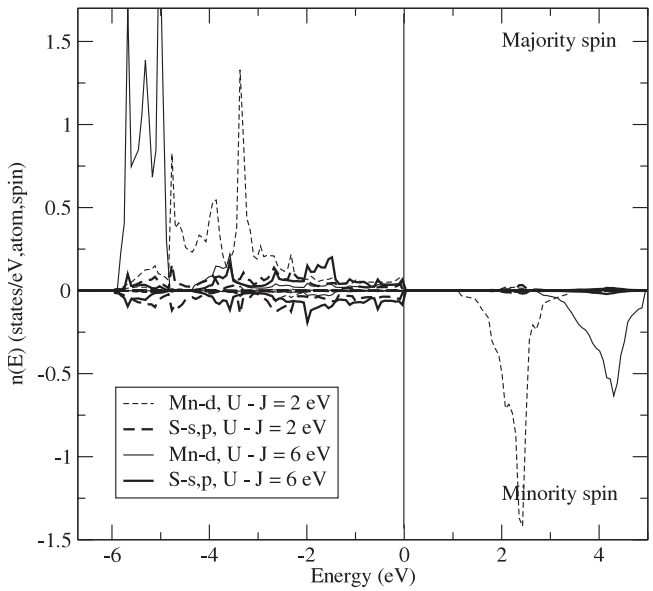

Figure 2. Spin-polarized DOS of the Mn d–S p band complex near the Fermi level in MnS calculated in the GGA + U for $U - J = 2$ and 6 eV (broken and full curves respectively).

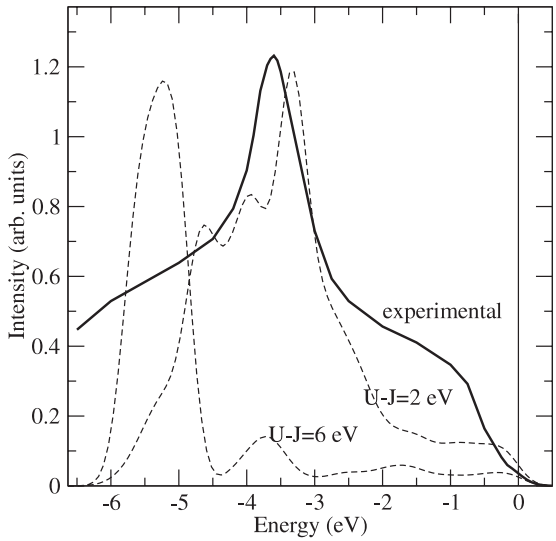

Figure 3. Measured valence-band photoemission spectrum of MnS ($h\nu = 40.8$ eV) and estimate of the photoemission spectra calculated as a weighted average of the partial DOSs with photoionization cross-sections from [36]. Calculations have been performed in the GGA + U, using different values of the on-site Coulomb interaction.

of 76.6 GPa (see [41]). Below $T_N = 48$ K, it is antiferromagnetic of type III with a magnetic moment of μ_{Mn} close to the Hund's-rule limit of 5 μ_B. GGA calculations [5] predicted MnS_2 to be a zero-gap semiconductor with a low-spin AFM type-III state with a magnetic moment of $\mu_{\mathrm{Mn}} = 1.4\ \mu_B$ and an equilibrium volume of 14.2 Å/atom. A high-spin AFM ground state

with magnetic moment of $\mu_{\mathrm{Mn}} = 3.8\ \mu_B$ could be found at a volume of 17.5 Å/atom, but the low-spin state was more stable. In the high-spin case, there is still a volume discrepancy of about 7%. The magnetic moment is underestimated by about 15%. The high-spin/low-spin transition is coupled to a structural distortion leading to shorter S–S distances in better agreement with experiment.

DFT + U calculations can stabilize the high-spin AFM ground state, and give better volume and magnetic moment estimations. Figure 4 shows the variation of volume, energy gap, magnetic moment and S–S dimer length with increasing $U - J$. In the LDA + U, full agreement with the experimental atomic volume cannot be achieved even with strong on-site interactions of U around 9 eV. The magnetic moment is not very accurately known, but at U around 6–7 eV the calculated moment is already only 10% below the limit set by Hund's rule. The observed width of the semiconducting gap is already reached at $U - J$ around 4 eV. Again in the GGA + U a much smaller value of the on-site potential of $U - J \sim 2$ eV is sufficient to get an atomic volume and bandgap in agreement with experiment. The internal structural parameter u fixing the length of the S–S dimers characteristic for the pyrite structure is found to be independent of U in both approximations and slightly larger than found in the experiment. At moderate U a high-pressure low-spin phase coexists with the stable high-spin phase at ambient conditions. This is illustrated in figure 5 displaying the volume dependence of the internal energy, the magnetic moment and the S–S distance for fixed $U - J$. For GGA + U and $U - J \sim 2$ eV, we find a discontinuous structural and magnetic phase transition at a critical pressure of $p_C \sim 11$ GPa, resulting in a volume change of $\Delta V \sim 3$ Å^3, a drop in the magnetic moment from $\mu_{\mathrm{Mn}} \sim 4$ to 1.6 μ_B and an increase of the S–S distances by about 0.12 Å. For larger U, the transition pressure increases ($p_C \sim 16$ GPa at $U - J = 3.5$ eV and GGA + U). At too small U, the low-spin phase is stabilized. In the LDA + U, this happens already at $U - J \sim 2$ eV, in the GGA + U only in the limit of very small U (cf figure 5 in [5]). At $U - J = 8$ eV on the other hand, the high-spin/low-spin transition is completely suppressed; even under a compression of ∼30% the magnetic moment is reduced only very slightly.

The electronic structure also shows a strong dependence on the on-site Coulomb potential. In the pyrite structure, each TM atom is surrounded by six sulfur atoms in a slightly distorted octahedral environment—in such an environment, the TM d band splits into the t_{2g} and e_g manifolds. The t_{2g} orbitals are almost perpendicular to the TM–S bonds, hence they are essentially non-bonding. The e_g orbitals extend along the direction of the Mn–S bonds and hybridize strongly with the S 3p states. In non-magnetic TMS_2 compounds the hybridization occurs in such a way that the TM e_g and S 3p levels form a broad complex of 20 bands just below the non-bonding t_{2g} band, in exact correspondence to the 20 bands that can be formed by the 3pσ, 3pπ and 3pπ^* states alone (see figure 6 in [5]). The anti-bonding TM e_g–S 3p hybrids form a group of 12 bands (four from S 3pσ^* and eight from the TM e_g states), separated by a narrow gap from the t_{2g} states [2]. In FeS_2, the Fermi level just falls into the gap separating the e_g and the antibonding TM e_g–S 3p bands, and the compound is a narrow-gap semiconductor and nonmagnetic. In paramagnetic MnS_2 the Fermi level falls just below the upper edge of the t_{2g} band and the compound is metallic with a high DOS at E_F. In the antiferromagnetic low-spin phase, the spin-polarized GGA calculations predict the Fermi level to fall into a very deep and narrow pseudo-gap in the t_{2g} minority band. The t_{2g} majority band is located at about −1.2 eV and completely filled; the Mn e_g–S 3p band complexes are hardly affected by the antiferromagnetic ordering [5]. In the high-spin phase, the GGA calculations predict an increased S sσ/sσ^* and S pσ/pσ^* bonding/anti-bonding splitting (caused by the reduced S–S dimer bond length) and a strongly reduced Mn d–S p hybridization. For the majority-spin states both the t_{2g} and e_g bands are fully occupied; for the minority-spin states both are

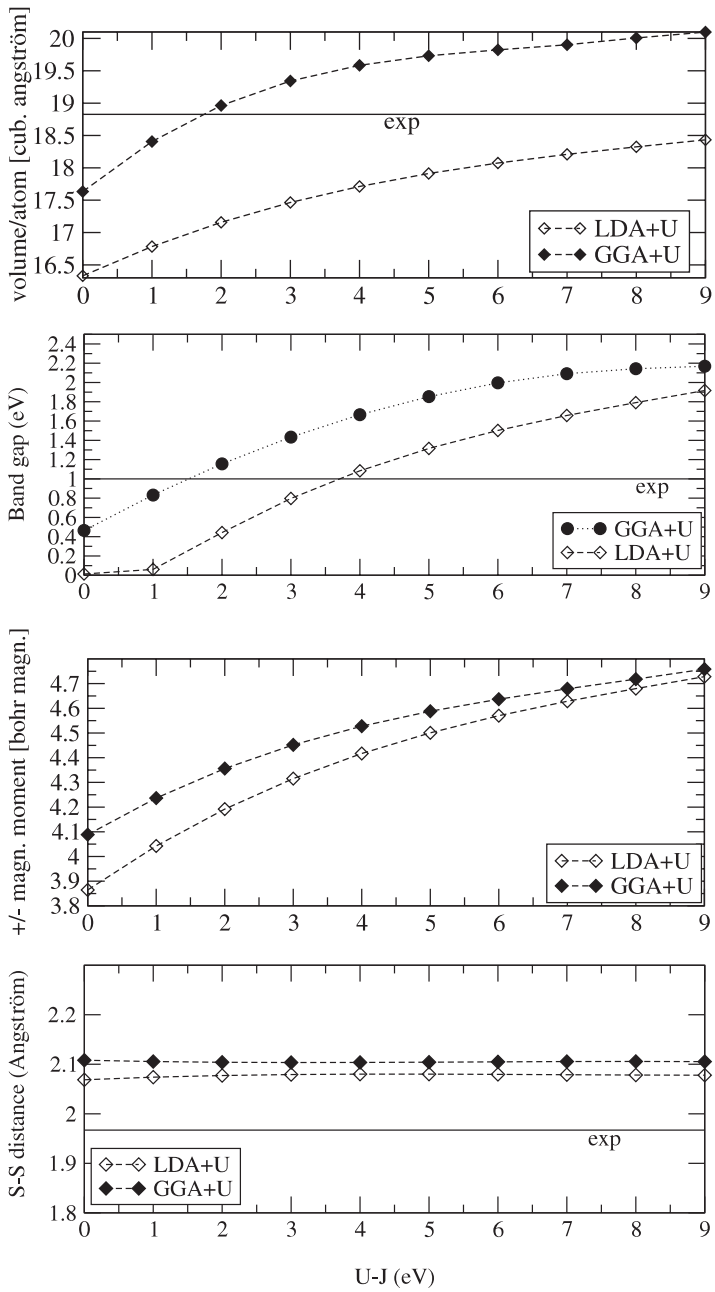

Figure 4. Volume, bandgap, magnetic moments and the S–S distance in MnS_2 plotted against different $U - J$ parameters. Horizontal lines mark the experimental value, if available.

empty. The Fermi level falls into a narrow (0.04 eV) gap between the occupied spin-up e_g and the empty spin-down t_{2g} states [5]. At a small to moderate value of the on-site interaction ($U - J \leqslant 3.5$ eV), the DOSs calculated in both the LDA + U and GGA + U are qualitatively similar to the spin-polarized GGA result (see figure 6), but even for $U - J \sim 3.5$ eV the

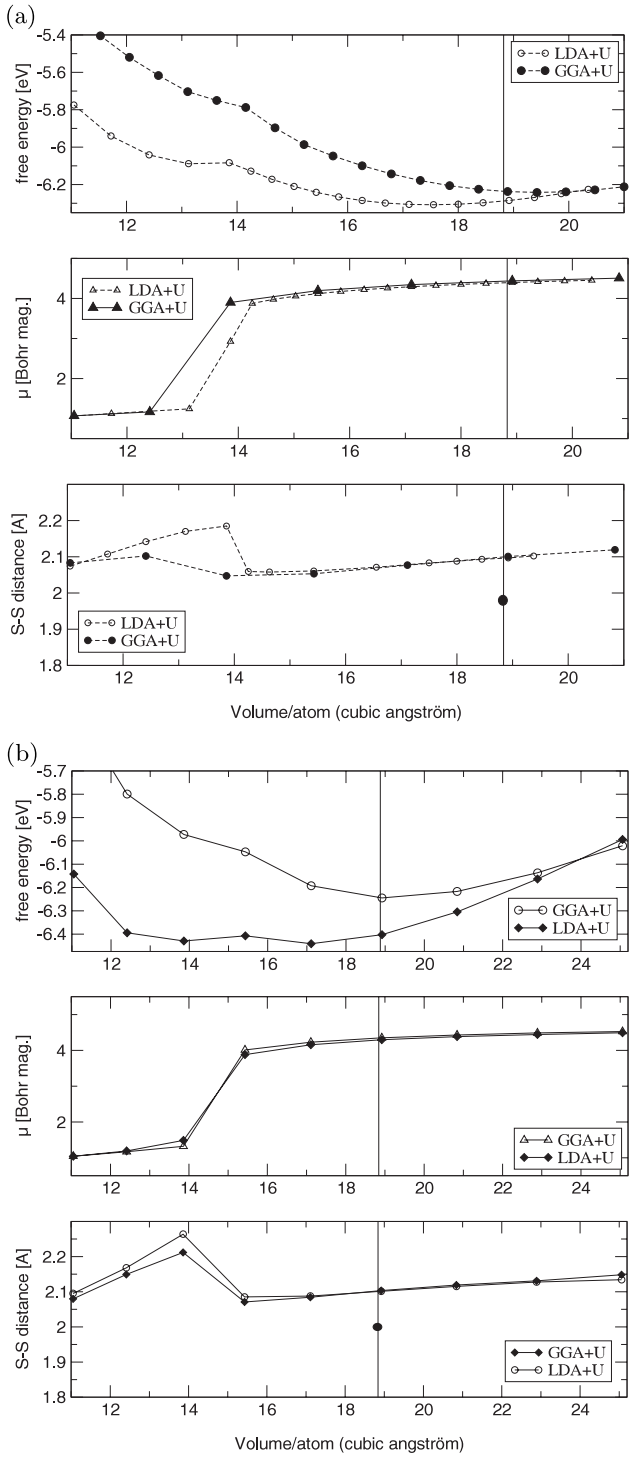

Figure 5. Energy, magnetic moments and the S–S distance in MnS_2 plotted against volume calculated in the LDA + U and GGA + U for (a) moderate ($U - J = 3.5$ eV) and (b) weak ($U - J = 2$ eV) correlation. The vertical line marks the experimental volume.

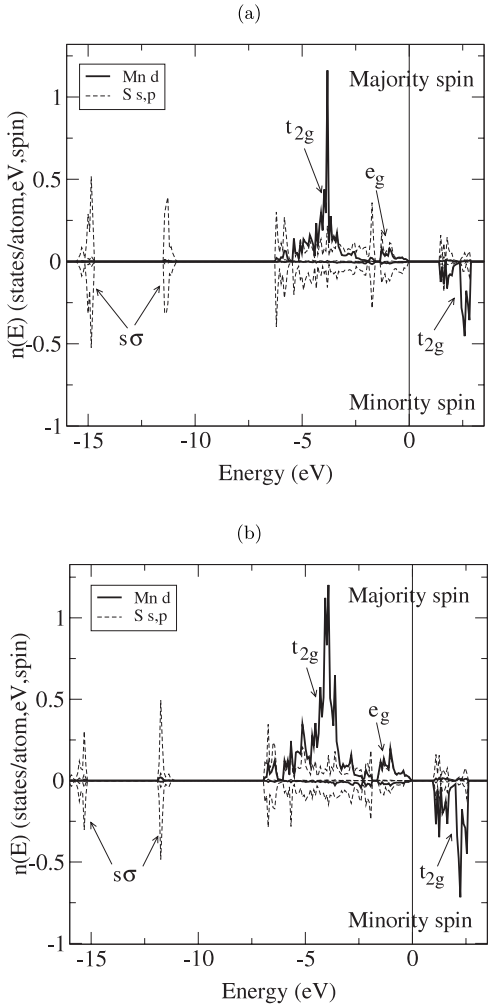

Figure 6. Density of states for MnS_2 calculated with GGA + U (a) and LDA + U (b), both with $U - J = 3.5$ eV.

main d-band peak is located at -3.7 eV, compared to -2.8 eV in the GGA. The fact that, for the same U, the DOSs calculated in the LDA + U and GGA + U differ only slightly should be noted. The remaining differences are due to the different equilibrium volumes, which lead to a somewhat smaller band-width in the GGA + U—this also helps to widen the bandgap. This underlines the fact that a consistent description of atomic and electronic properties can only be achieved if gradient corrections are applied before introducing the on-site Coulomb-potential. If the intra-atomic correlation is very strong, the Mn d band is pushed even below the lower edge of the S 3p band and the hybridization is reduced almost to zero. Hence valence-band photoelectron spectroscopy could help to assess the strength of correlation effects in MnS_2. In addition, high-pressure experiments exploring the possibility of a high-spin/low-spin transition could help in assessing a realistic value of U in MnS_2. Again it is important to emphasize that the GGA + U offers a more consistent picture than the LDA + U.

5. Fe monosulfide

At low temperature and ambient pressure, FeS assumes the troilite structure and is an antiferromagnetic insulator ($E_g = 0.04$ eV) with a magnetic moment of $\mu_{\mathrm{Fe}} \sim 4\ \mu_B$ [37]. At a temperature of $T_\alpha = 420$ K, FeS transforms to the MnP-type structure, but remains antiferromagnetic. The magnetic transition at a Néel temperature of $T_N = 593$–598 K is accompanied by a structural transformation to the NiAs structure. The troilite structure can be derived from the more symmetric NiAs structure by small displacements of the Fe and S atoms. Both the MnP and NiAs phases are stabilized under compression. Under a pressure of 3.4 GPa, the temperature for the troilite to MnP transition is lowered to 298 K; the NiAs phase is also stabilized under compression.

The GGA calculations correctly reported the troilite structure to be more stable, but in a low-spin antiferromagnetic state of $\mu_{\mathrm{Fe}} = 1.8\ \mu_B$ [5]. Furthermore, the calculated equilibrium volume is underestimated by about 10%. The pressure-induced phase change to the NiAs structure was correctly predicted and the equilibrium volume of the non-magnetic ground state of FeS in the NiAs structure is underestimated by about 17%. The calculated antiferromagnetic ground state of FeS in the NiAs structure with an Fe magnetic moment of $2.7\ \mu_B$ [5], where the equilibrium volume is only 5% below the experimental value, is only metastable; the energy difference is ~ 30 meV/atom.

In the DFT + U calculations we expect an improvement in the equilibrium volume predictions for the troilite structure, including the correct gap opening and the stabilization of the high-spin antiferromagnetic state. Figure 7 shows the variation of the equilibrium volume, the magnetic moment, the bandgap, the structural energy difference and the c/a-ratio for both troilite and NiAs-type FeS as a function of $U - J$. The equilibrium volumes for both phases already agree with experiment at a moderate value of the on-site Coulomb interaction ($U - J \sim 3.5$ eV in the LDA + U, $U - J \sim 1$ eV in the GGA + U); a semiconducting gap opens at $U - J \sim 1$ eV in both approximations. On the other hand, although a moderate value of U is sufficient to create a high-spin ground state, the 'experimental' value of the magnetic moment (which is identical with the upper limit set by Hund's rule) is not reached even for very strong correlation effects. Coey and Roux-Buisson [37] have estimated the magnetic moment of $\mu_{\mathrm{Fe}} \simeq 4\ \mu_B$ on the basis of Mössbauer hyperfine field data only. We suspect that our value $\mu_{\mathrm{Fe}} \simeq 3.3\ \mu_B$ calculated for the values of U producing the correct equilibrium volume is a more realistic estimate. We also emphasize that a too strong on-site Coulomb repulsion leads to a structural distortion characterized by a too low axial ratio.

Figures 8 and 9 show the variation of the total energy and of the magnetic moment of the two competing FeS phases calculated at the optimized values of U as a function of volume using either the LDA + U (figure 8) or the GGA + U (figure 9). From the double-tangent construction to the energy versus volume curve a pressure-induced troilite to NiAs transition is predicted in the LDA + U ($U - J = 3.8$ eV) at $p_C = 18.5$ GPa; the transition is first order and accompanied by a volume change of $\Delta V = 0.54$ Å^3. In the GGA + U ($U - J = 2$ eV) and at the value of U optimizing the agreement of most properties with experiment, the transition pressure is reduced to $p_C \sim 6$ GPa and the volume discontinuity to $\Delta V = 0.3$ Å^3. From x-ray diffraction it has been estimated that the pressure-induced phase transition occurs at a volume compression of ∼15%. This is in good agreement with the GGA + U result, whereas in the LDA + U the transition occurs only at substantially higher compression. No substantial change of the magnetic moment occurs at the transition, whereas the GGA calculations predicted a transition from antiferromagnetic troilite to a nonmagnetic NiAs-type phase.

Figures 10 shows the electronic DOS of troilite, calculated in the LDA + U for $U - J \simeq 3.8$ eV and in the GGA + U for $U - J = 2$ eV. In contrast to the spin-polarized GGA

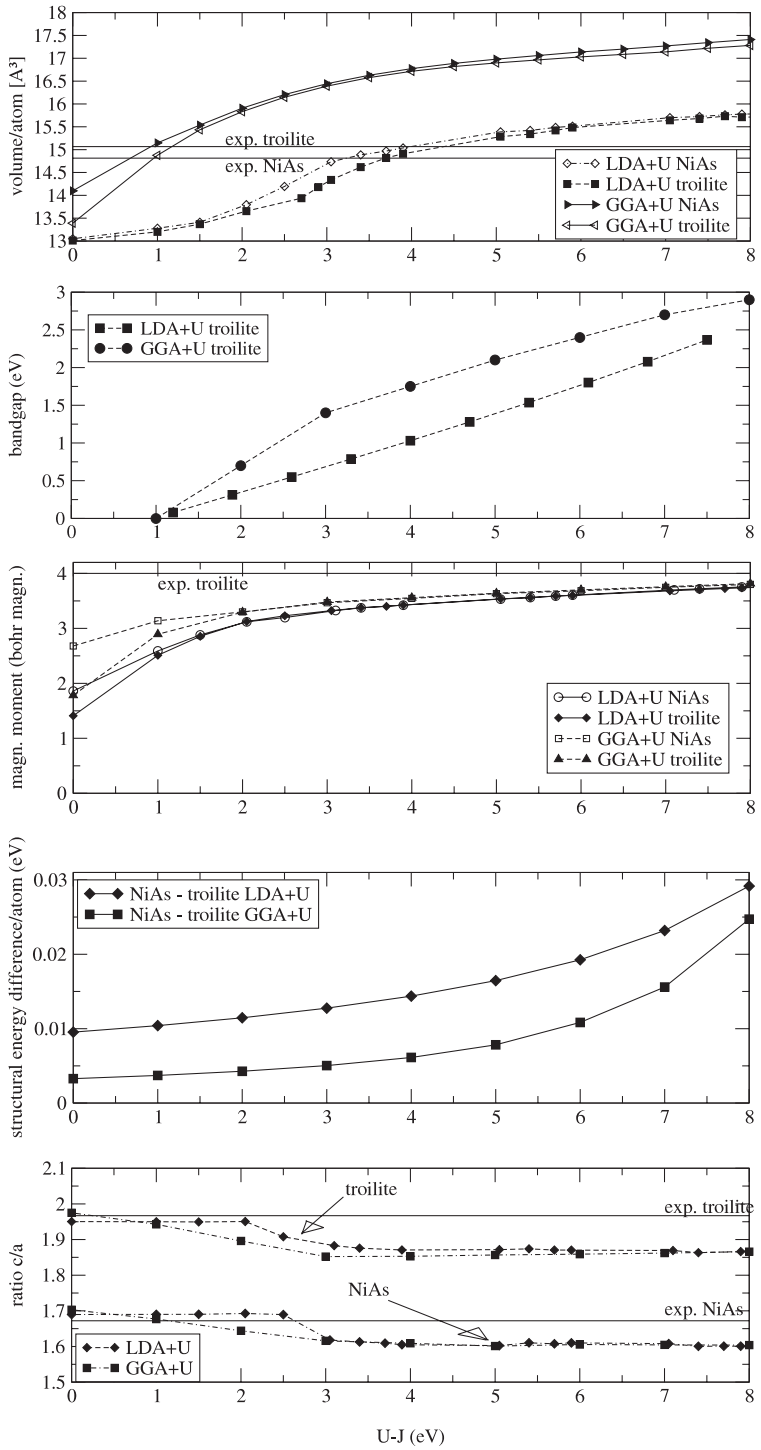

Figure 7. Volume, bandgap, magnetic moment, structural energy difference and c/a-ratio of the troilite- and NiAs-type phases of FeS plotted against $U - J$. The experimental values are indicated by horizontal lines.

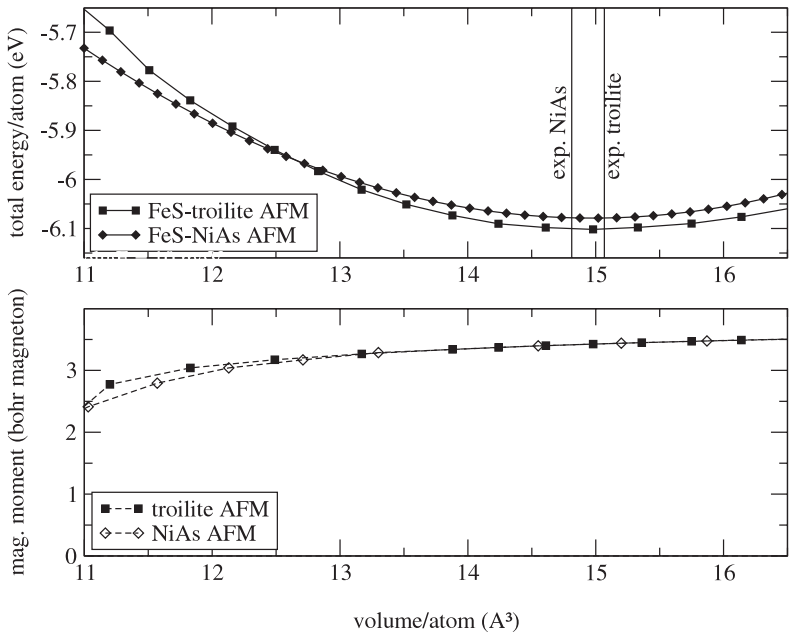

Figure 8. LDA + U: energy and magnetic moment plotted against volume for antiferromagnetic FeS in the troilite and NiAs structures, calculated at $U - J = 3.8$ eV.

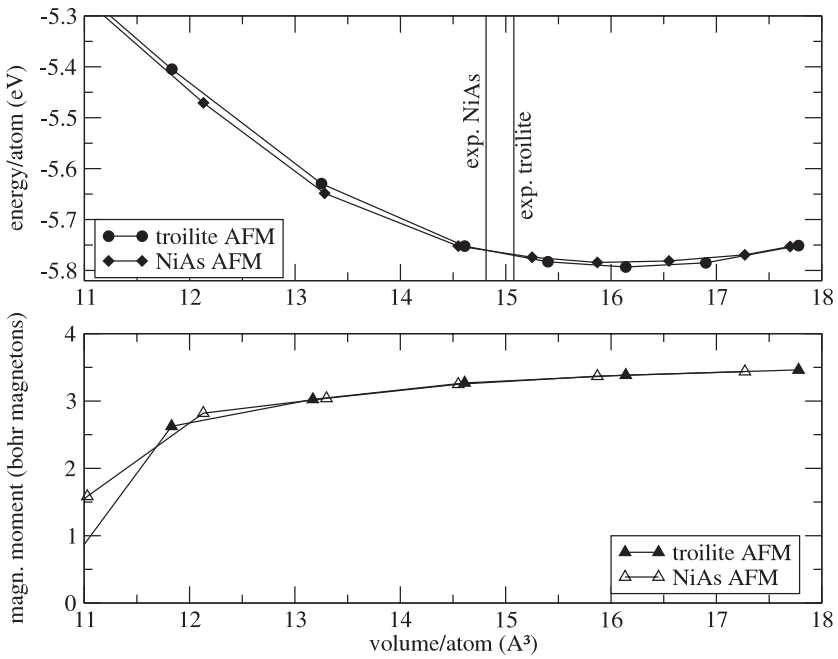

Figure 9. GGA + U: energy and magnetic moment plotted against volume for antiferromagnetic FeS in the troilite and NiAs structures, calculated at $U - J = 2$ eV.

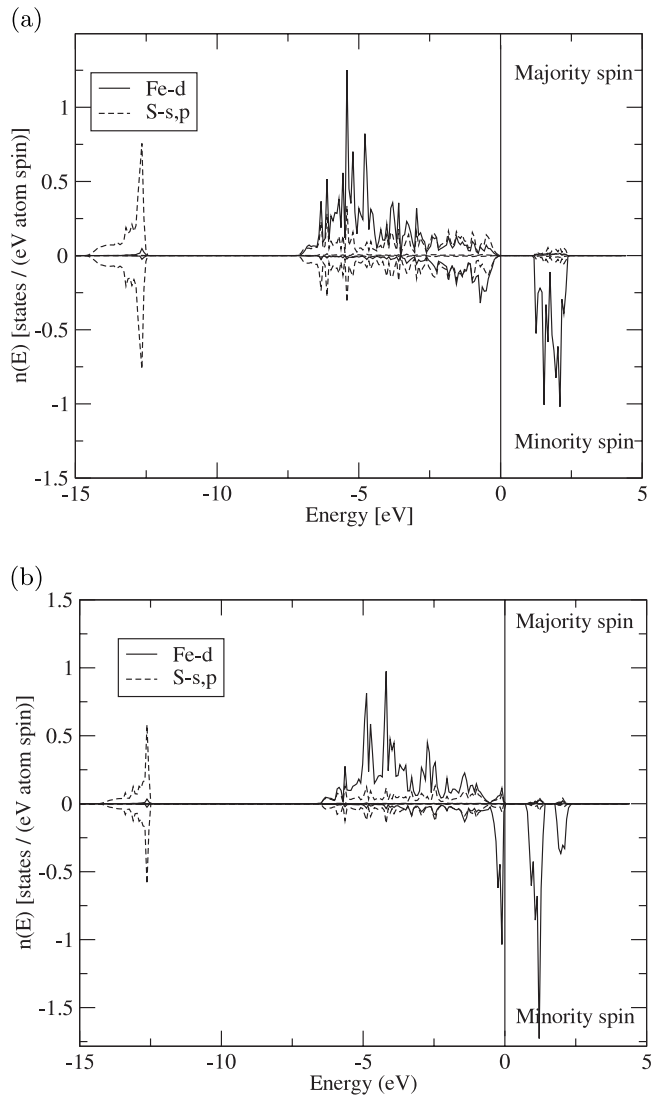

Figure 10. The DOS for the antiferromagnetic FeS in the troilite structure calculated with LDA + U ($U - J = 3.8$ eV) (a) and GGA + U ($U - J = 2$ eV) (b).

calculations which find troilite to be metallic, with a substantial overlap of the majority and minority Fe 3d bands, the LDA + U and GGA + U calculations predict troilite to be a narrow gap semiconductor with a gap of ∼1 eV. The vanishing DOS at the Fermi level is in agreement with electronic specific-heat measurements. From ultraviolet photoemission (UPS) and x-ray inverse photoemission experiments (XIPES), Shimada *et al* [38] estimated a very low gap width of $E_g \sim 0.04$ eV. A comparison between the experimental and theoretical spectra is shown in figure 11—the theoretical spectra are approximated by the average partial DOS, weighted with the photoionization cross-sections. The calculated spectra are dominated by the contribution of the Fe 3d bands. The other contributions are more than a factor of 30 lower. Figure 11 shows that in the GGA + U and for small $U \sim 2$ eV the near Fermi edge part of the

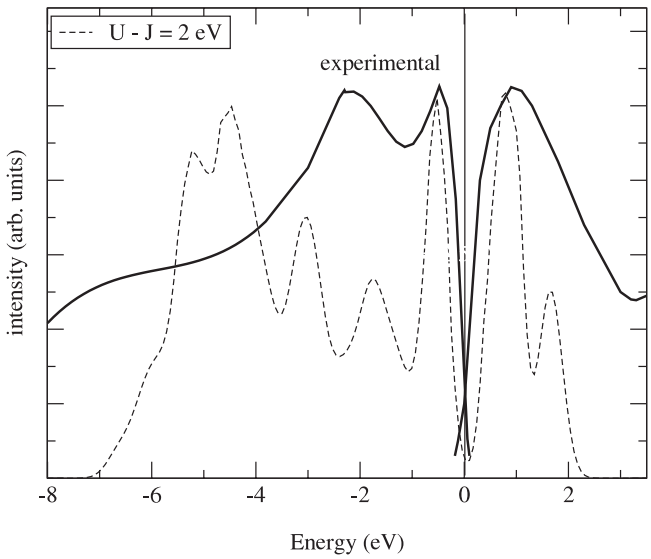

Figure 11. Valence band photoemission spectra at 40.8 eV for FeS by [38] (bold curve) together with an estimate of the photoemission spectra calculated from the density of states (from GGA + U calculations) with photoionization cross-sections.

spectra dominated by the minority-spin bands is rather well reproduced. The Fe 3d majority bands, however, appear to have been shifted to too high binding energies.

6. Conclusions

We have reported results of DFT + U calculations of a wide range of physical properties of some TMSs influenced by electronic correlation effects. We have found that when the on-site Coulomb repulsion is added to a purely local DFT Hamiltonian described in an LSDA, a large value of U is necessary to compensate for the overbinding characteristic for the LSDA and for the underestimation of the magnetic moment and magnetovolume effects so as to bring the equilibrium atomic volume into agreement with experiment. For the one-electron energies, this large on-site Coulomb potential leads to a too large exchange splitting and a too wide energy gap. Due to the shift of the occupied states to higher binding energies, the calculated one-electron energies disagree with the photoemission spectra. As shown earlier [5], the spin-polarized GGA largely, but not completely, corrects for the underestimate of the atomic volume. If the on-site Coulomb repulsion is added to the GGA Hamiltonian, a modest value of U is sufficient to close the gap between the theoretical and experimental volumes. With the weaker correlation effects, a good description of structural stability, the magnetic properties and of the electronic spectrum can be achieved as well. Our results suggest that the DFT + U method should be used in conjunction with gradient corrections to the local functionals. Preliminary results confirm that this conclusion also holds for other materials with strong electronic correlations.

Acknowledgment

This work has been performed within the Science College ‘Computational Materials Science’ supported by the Austrian Science Fund (FWF) under project no W004.

References

[1] Topsoe H, Clausen B S and Massoth F 1996 *Hydrotreating Cataylsis (Springer Series in Science and Technology vol 11)* (Berlin: Springer)
[2] Raybaud P, Kresse G, Hafner J and Toulhoat H 1997 *J. Phys.: Condens. Matter* **9** 11085
[3] Harris S and Chianelli R R 1984 *J. Catal.* **86** 400
Harris S and Chianelli R R 1986 *J. Catal.* **98** 17
[4] Raybaud P, Kresse G, Hafner J and Toulhoat H 1997 *J. Phys.: Condens. Matter* **9** 11107
[5] Hobbs D and Hafner J 1999 *J. Phys.: Condens. Matter* **11** 8197
[6] Ansisimov V I, Zaanen J and Andersen O K 1991 *Phys. Rev.* B **44** 943
[7] Anisimov V I, Solovyev I V, Korotin M A, Czyzyk M T and Sawatzky G A 1993 *Phys. Rev.* B **48** 16929
[8] Anisimov V I, Aryasetiawan F and Lichtenstein A I 1997 *J. Phys.: Condens. Matter* **9** 767
[9] Dudarev S L, Botton G A, Savrasov S Y, Humphreys C J and Sutton A P 1998 *Phys. Rev.* B **57** 1505
[10] Kotani A and Yamazaki T 1992 *Prog. Theor. Phys. Suppl.* **108** 117
[11] Solovyev I V, Dederichs P H and Anisimov V I 1994 *Phys. Rev.* B **50** 16861
[12] Lichtenstein A I, Anisimov V I and Zaanen J 1995 *Phys. Rev.* B **52** R5467
[13] di Salvo F J and McMillan W L 1977 *Electron–Phonon Interaction and Phase Diagrams* ed T Riste (New York: Plenum) p 107ff
[14] Blöchl P E 1994 *Phys. Rev.* B **50** 17953
[15] Kresse G and Joubert D 1999 *Phys. Rev.* B **59** 1758
[16] Bengone O, Alouani M, Blöchl P and Hugel J 2000 *Phys. Rev.* B **62** 16392
[17] Shick A B, Liechtenstein A I and Pickett W E 1999 *Phys. Rev.* B **60** 10763
[18] Kohn W and Sham L J 1964 *Phys. Rev.* **140** A1133
[19] Jones R O and Gunnarsson O 1989 *Rev. Mod. Phys.* **61** 689
[20] Kresse G and Hafner J 1993 *Phys. Rev.* B **47** 588
[21] Kresse G and Hafner J 1994 *Phys. Rev.* B **49** 14251
[22] Kresse G and Furthmüller J 1996 *Phys. Rev.* B **54** 11169
[23] Kresse G and Furthmüller J 1996 *Comput. Mater. Sci.* **6** 15
[24] Perdew J P and Zunger A 1981 *Phys. Rev.* B **23** 5048
[25] Ceperley D M and Alder B J 1980 *Phys. Rev. Lett.* **45** 566
[26] Vosko S H, Wilk L and Nusair M 1980 *Can. J. Phys.* **58** 1200
[27] Perdew J P, Chevary J A, Vosko S H, Jackson K A, Pederson M R, Singh D J and Fiolhais C 1992 *Phys. Rev.* B **46** 6671
[28] Wood D M and Zunger A 1985 *J. Phys. A: Math. Gen.* **18** 1343
[29] Johnson D D 1988 *Phys. Rev.* B **38** 12087
[30] Pulay P 1980 *Chem. Phys. Lett.* **73** 393
[31] Monkhorst H J and Pack J D 1976 *Phys. Rev.* B **13** 5188
[32] Hines R I, Allen N L, Bell G S and Mackrodt W C 1997 *J. Phys.: Condens. Matter* **9** 7105
[33] Tappero R, D'Arco P and Lichanot A 1997 *Chem. Phys. Lett.* **173** 83
[34] Tappero R and Lichanot A 1998 *Chem. Phys. Lett.* **236** 97
[35] Sato H, Mihara T, Furuta A, Ueda Y, Namatame H and Taniguchi M 1996 *J. Electron Spectrosc. Relat. Phenom.* **78** 87
[36] Yeh J J and Landau I 1985 *At. Data Nucl. Data Tables* **32** 1
[37] Coey J M D and Roux-Buisson H 1979 *Mater. Res. Bull.* **14** 711
[38] Shimada K, Mizokawa T, Mamiya K, Saitoh T, Fujimori A, Ono K, Kakizaki A, Ishii T, Shirai M and Kamimura T 1998 *Phys. Rev.* B **57** 8845
[39] Womes M, Karnatak R C, Esteva J M, Lefebvre I, Allan G, Olivier-Fourcade J and Junas J C 1997 *J. Phys. Chem. Solids* **58** 345
[40] Brostigen G and Kjekshus A 1970 *Acta Chem.* **5** 2993
[41] Tappero R, Baraille I and Lichanot A 1998 *Phys. Rev.* B **58** 1236
[42] Izyumov Yu A 1995 *Sov. Phys.–Usp.* **38** 385